



## OPEN Study on the bonding behavior of concrete-filled aluminum alloy tube

Fang-ling Liu<sup>1</sup>, Jing-Xuan Wang<sup>1,2</sup>✉ & Shan Gao<sup>3</sup>✉

Aluminum alloy has been widely used in modern engineering structures due to its good corrosion resistance, light-weight, convenient processing, and recyclability. To study the bonding behavior of concrete-filled aluminum alloy tubes (CFAT) columns and obtain the bond strength formula and bond-slip constitutive model of CFAT, the push-out tests of three circular and three square CFAT specimens were conducted. The failure patterns, load-slip/strain curves and the stress distribution of the stubs were investigated. The results show that the longitudinal strain of both square and circular CFAT specimens increased from the loading end towards the free end. Based on the elastic assumption, the interfacial bond stress of CFAT was calculated. The ultimate bond strength for the circular specimens ranged from 0.77 to 1.77 MPa, whilst the square ones ranged from 0.22 to 0.51 MPa. As the section size increased, the bond strength of CFAT gradually decreased. When the diameter-to-thickness ratio or the width-to-thickness ratio increased from 48.0 to 80.0, the ultimate bond strength of the square and circular specimens decreased by 67.2% and 67.5%, respectively. Additionally, a calculation formula for the ultimate bond strength of CFAT is proposed. Based on the proposed formula for characteristic points, a bond-slip constitutive model for CFAT columns is proposed and validated. Finally, based on the verified bond-slip constitutive model of CFAT, the finite element (FE) models of spring element and cohesive model are established, respectively. The modeling result of the spring element is more accurate and the calculation efficiency is higher. However, the modeling process is complex.

**Keywords** Concrete-filled aluminum alloy, Bond behavior, Bond strength formula, Bond-slip constitutive model, Numerical simulation

In the background of the rapid development in the construction industry, how to effectively address the issues of steel corrosion, reduce maintenance costs in the later stages, and lighten the structural weight has become a topic of widespread concern among scholars. Currently, there are several measures available, as shown in Fig. 1. Firstly, by spraying anti-corrosion materials on the surface of steel, its corrosion resistance can be enhanced. Secondly, preset the corrosion allowance in the design phase to ensure the long-term stability of the steel during its use. Additionally, the use of new materials such as stainless steel<sup>1,2</sup>, GFRP<sup>3</sup>, and aluminum alloy tubes<sup>4-6</sup> can be considered as alternatives to traditional steel to reduce the risk of corrosion and achieve lightweight design. Compared with steel tubes, aluminum alloy tubes are becoming increasingly popular in research due to their excellent corrosion resistance, lightweight nature, and recyclability. At present, extensive research has been conducted on the axial compressive performance of concrete-filled aluminum alloy tube (CFAT) columns. The research covered the filling of aluminum tubes with ordinary concrete<sup>4-13</sup>, coral concrete<sup>14-16</sup>, geopolymer concrete<sup>17</sup>, fiber concrete<sup>18</sup>, and sea-sand concrete<sup>19-21</sup>. These studies indicate that filling aluminum alloy tubes with various types of concrete materials can provide better mechanical properties and durability under a range of construction requirements, while also meeting the building's demand for material performance. This approach can reduce environmental impact to a certain extent and promote the construction industry towards a more environmentally friendly and sustainable direction. Furthermore, several researchers have investigated the axial compression characteristics of concrete-filled double skin aluminum alloy tubular<sup>19,22-24</sup>, inner steel tube outer aluminum alloy tubes concrete columns<sup>25,26</sup>, as well as CFRP confined concrete filled aluminum alloy tube columns<sup>20,27,28</sup>. By optimizing the design of composite structures and leveraging the advantages of various materials, the overall performance of CFAT columns in complex environments can be enhanced.

The bonding between the metal tube and concrete is the basis to ensure the overall force of the member. Once there is debonding or relative slippage between the metal tube and the concrete, it will affect the mechanical

<sup>1</sup>School of Civil Engineering, Lanzhou University of Technology, Lanzhou 730050, People's Republic of China.

<sup>2</sup>Western Center of Disaster Mitigation in Civil Engineering of Ministry of Education, Lanzhou University of Technology, Lanzhou 730050, People's Republic of China. <sup>3</sup>Key Lab of Structures Dynamic Behavior and Control of the Ministry of Education, Harbin Institute of Technology, Harbin 150090, People's Republic of China. ✉email: cewangjx@lut.edu.cn; gaoshan@hit.edu.cn

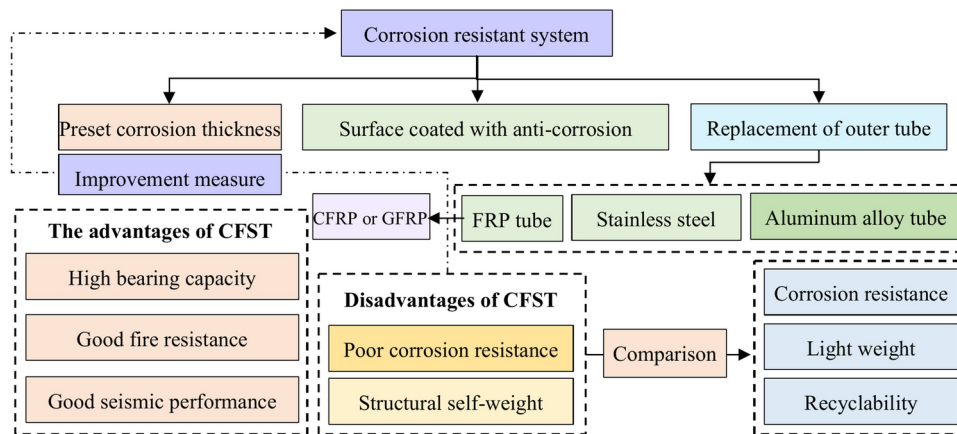


**Fig. 1.** Corrosion resistant system.

performance of the members and the effective transfer of forces at the beam-column joints. Therefore, studying the bond performance between the metal tube and the concrete is of great significance. The research on the interfacial bond behavior of concrete-filled steel tubes (CFST) is relatively mature at present. As research has deepened, studies have been conducted on the bonding behavior of CFST columns under various conditions such as normal temperature<sup>29–32</sup>, low temperature<sup>33</sup>, temperature rise<sup>34</sup>, post-fire<sup>35–38</sup>, and freeze–thaw cycles<sup>39,40</sup>. Some relatively consistent understandings have been reached: the bond behavior of circular specimens is significantly higher than that of square specimens. As the diameter to thickness ratio ( $D/t$ ) or width to thickness ratio ( $B/t$ ) increases, the bond strength decreases. Low temperature environments and freeze–thaw cycles can reduce the interfacial bond strength of CFST. However, under heating conditions, the interfacial bond strength can initially increase, but excessively high temperatures may also cause it to decrease. Furthermore, in order to improve the mechanical properties of CFST and reduce the consumption of natural resources, researchers has also been conducted on the bond behavior of new concrete materials filled into steel tubes, such as fiber-reinforced concrete<sup>41</sup>, high-performance concrete<sup>42</sup>, and recycled concrete<sup>43,44</sup>. Meanwhile, researches on the interfacial bonding performance between concrete-filled stainless steel tube<sup>1,2</sup> and CFAT<sup>45,46</sup> are also emerging. Xiang<sup>45</sup> studied the effect of freeze–thaw cycles on the interfacial bond strength between circular aluminum alloy tubes and concrete, and compared it with CFST columns of the same size. The results showed that the bond strength of the CFAT columns ranged from 1.34 to 1.67 MPa, while the bond strength of the CFST columns was between 0.82 and 1.0 MPa. This was because the corrosion reaction of the steel tube weakened the chemical bond between the steel tube and the concrete. Zhu<sup>46</sup> conducted research on circular CFAT after high temperature exposure, using concrete strength, slenderness ratio, and temperature as varying parameters. The results showed that the ultimate bond strength between the aluminum alloy tube and the concrete increased with the increase in temperature and concrete strength, but decreased with the increase in slenderness ratio. In summary, the interfacial bonding between the aluminum alloy tube and concrete is the foundation for their cooperative performance. Existing research efforts have primarily focused on the bonding behavior of circular cross-section CFAT, while there are limited reports of square cross-section.

Therefore, this paper investigates the bonding behavior of CFAT with square and circular columns, using the diameter-to-thickness ratio ( $D/t$ ) and width-to-thickness ratio ( $B/t$ ) as the main parameters. A comparative observation was made on the failure phenomena and strain distributions of the two types of cross-sectional specimens and proposes a formula for calculating the bond strength and a bond-slip constitutive model of CFAT. Meanwhile, numerical models using spring elements and cohesion models are established respectively through ABAQUS to verify the applicability of these two modeling methods for the bonding behavior of CFAT columns.

## Experimental programs

### Specimen design

A total of six concrete-filled aluminum alloy tube (CFAT) push-out specimens were designed. The aluminum alloy tube designed in this paper is obtained by extrusion. Based on the variation pattern of CFST<sup>47</sup>, this paper designed specimens with cross-sectional dimensions of 120 mm, 150 mm, and 200 mm to investigate the influence of cross-sectional size changes on the bond performance of CFAT. Meanwhile, to ensure that the concrete at the free end can slide during the push-out test, a 50 mm section of the aluminum alloy tube at the end was left unfilled with concrete during the pouring process. The length-to-diameter ratio ( $L/D$ ) or length-to-width ratio ( $L/B$ ) of all specimens is 3.0. To prevent premature cracking of the aluminum alloy tube at the column head and foot, three layers of 50 mm-wide carbon fiber reinforced polymer (CFRP) cloth were bonded to both ends of the specimens. Detail parameters of specimens are shown in Table 1.

The numbering rule in the table is as follows: The first letter stands for CFAT. The second letter represents the section form, C represents the circular cross-section, S represents the square cross-section. The third letter S stands for short columns. T stands for pushing out the specimen.

Cross-section	Specimens	L/D or L/B	D or B (mm)	t (mm)	D/t or B/t	Aluminum alloy ratio $\alpha$ (%)	Confinement coefficient $\theta$
	CCS120×2.5T	3.0	120	2.5	48.0	9.4	0.72
	CCS150×2.5T	3.0	150	2.5	60.0	7.3	0.57
	CCS200×2.5T	3.0	200	2.5	80.0	5.4	0.43
	CSS120×2.5T	3.0	120	2.5	48.0	4.8	0.59
	CSS150×2.5T	3.0	150	2.5	60.0	3.7	0.46
	CSS200×2.5T	3.0	200	2.5	80.0	2.7	0.34

**Table 1.** Detail parameter of specimens.

Cross section	$f_{0.1}$ (MPa)	$f_{0.2}$ (MPa)	$f_u$ (MPa)	$E_a$ (GPa)	Poisson's ratio $\mu_s$	Elongation $\delta$ (%)	Yield point strain $\epsilon_y$	Strain hardening index $n$
Circular	234.7	238.8	260.0	69,402	0.318	8.03	0.00546	43.41
Square	191.6	193.6	231.5	68,694	0.347	9.94	0.00489	21.85

**Table 2.** Material properties of aluminum alloy.

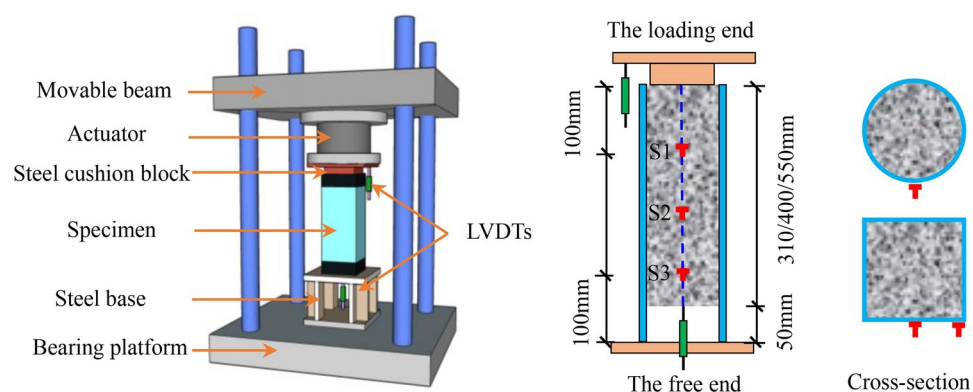


**Fig. 2.** Loading device and measuring point arrangement.

### Material properties

The aluminum alloy tube was selected to be of the 6061-T6. The mechanical properties such as the elastic modulus  $E_s$ , the strength corresponding to 0.001 residual strain  $f_{0.1}$ , the yield strength  $f_{0.2}$  (taking the stress corresponding to 0.2% residual deformation as the yield strength of the aluminum alloy), the ultimate tensile strength  $f_u$ , Poisson's ratio  $\mu_s$ , and elongation were measured from four standard specimens selected from square and circular aluminum alloy tubes respectively. The data are presented in Table 2.

According to GB 50936-2014<sup>48</sup>, the concrete strength inside the steel tube of a concrete-filled steel tubular column must not be less than C30. Additionally, previous studies<sup>4-6</sup> have shown that C40 concrete exhibits good compatibility with 6061-T6 aluminum alloy tubes and has been widely used in engineering applications. Therefore, C40 concrete was selected for use in this study. According to GB/T 50081-2019<sup>49</sup>, the measured axial compressive strength  $f_{co}$  and elastic modulus  $E_c$  of the concrete were 29.7 MPa and 25.6 GPa, respectively. The elastic modulus  $E_f$  and ultimate tensile stress  $\sigma_f$  of the CFRP were 240 GPa and 3667.5 MPa, respectively. Thickness  $t = 0.167$  mm, elongation  $\delta_c = 1.65\%$ .

### Loading device

The test was conducted on a 5000kN servo-hydraulic universal testing machine as shown in Fig. 2. Before the test begins, the concrete surface of the loading end of the specimens shall be polished to be smooth, and a steel cushion block shall be set. The edge of the cushion block should be 10 mm away from the inner surface of the aluminum alloy tube to ensure effective application. In order to measure the displacement of the concrete at the free end of the specimen being tested, a specially designed steel base has been created to hold the displacement meter.

## Experimental results and analysis

### Failure patterns

Figure 3 shows the failure phenomenon of the specimen. At the loading end, crescent-shaped damage mainly occurred at the boundary between the circular concrete and the aluminum alloy tube, whilst corner damage appears at the boundary of the square concrete. In the CSS150×2.5 T specimen, the surface concrete adhered to

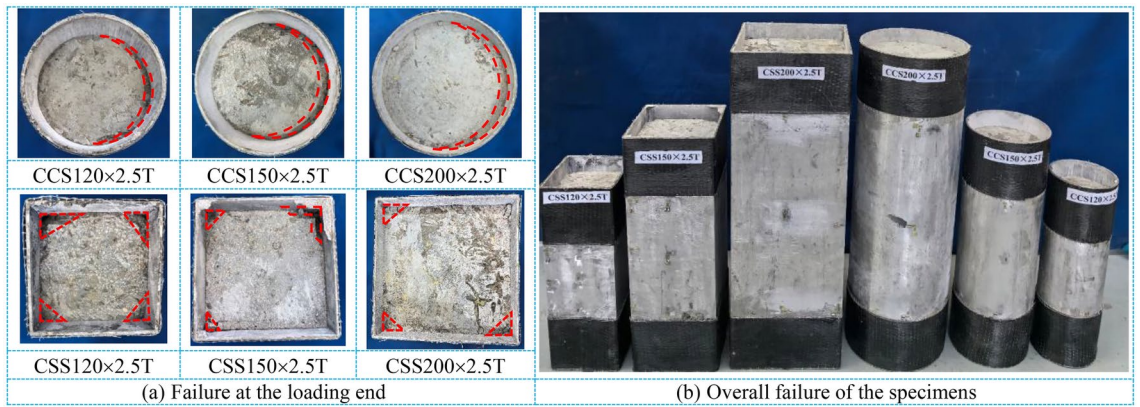


Fig. 3. The failure patterns of the specimen.

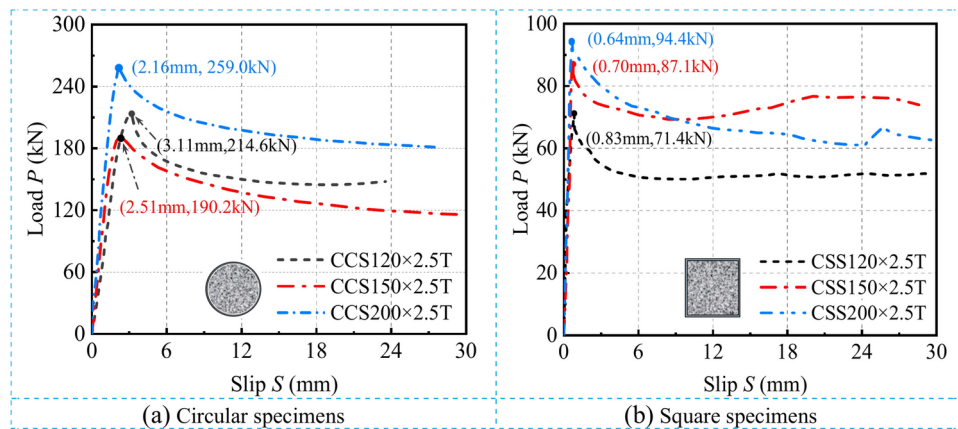


Fig. 4. Load-slip ( $P$ - $S$ ) relationship curves.

the corners, whilst there was little damage in the middle of the section. The degree of damage to the boundary of the core concrete in both types of sections decreases as the section size increases. From Fig. 5, it is observed that the smaller the section, the greater the bond stress. Meanwhile, vertical white stripes appeared on the inner wall of the aluminum alloy tube at the end, with relatively uniform scratch distribution on the circular tube and the most prominent scratches at the corners of the square tube.

### Load-slip relationship curves

Figure 4 shows the load-slip ( $P$ - $S$ ) relationship curves measured under the loading system. From the  $P$ - $S$  curves, it can be preliminarily observed that the ultimate load values of the circular specimens were all higher than those of the square specimens, and the corresponding slip values when bond failure occurs in the circular specimens were also greater than those in the square specimens. Before reaching the peak point, the rate of increase for the square-section specimens was significantly faster than that for the circular specimens. In the descending segment, there are no obvious fixed trend in the curves.

### Bond strength-slip relationship curves

Figure 5 shows the bond strength-slip ( $\tau$ - $S$ ) relationship curves calculated using Eq. (1). The ultimate bond strength ( $\tau_u$ ) of circular specimens ranges from 0.77 to 1.77 MPa, whilst square specimens range from 0.22 to 0.51 MPa. When the thickness of the specimens remains consistent, the smaller the cross-section of the specimens, the greater the ultimate bond strength ( $\tau_u$ ), the corresponding bond slip ( $S_u$ ) was also larger.

$$\tau = \frac{P}{A} \tag{1}$$

where  $\tau$  is the average bond stress between the aluminum alloy tube and the concrete, which was currently defined as the bond strength in research.  $P$  is the push load value, and  $A$  is the contact area between the aluminum alloy tube and the concrete.

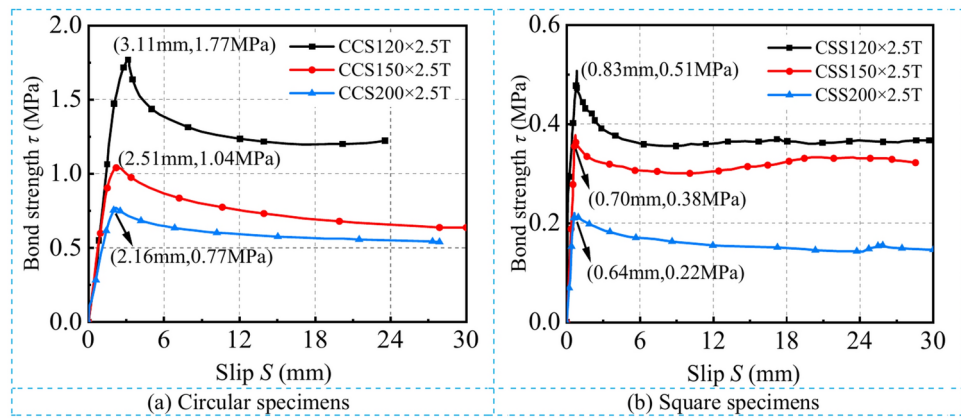


**Fig. 5.** Bond strength-slip ( $\tau$ - $S$ ) relationship curves.

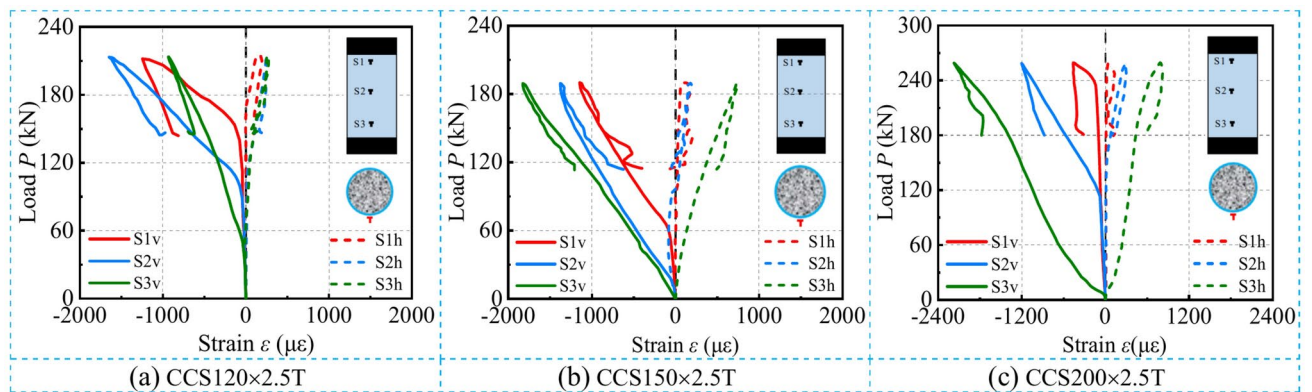


**Fig. 6.** Load-strain relationship curves of the circular specimens.

### Load-strain relationship curves

The load-strain ( $P$ - $\epsilon$ ) relationship curves of the circular specimen as shown in Fig. 6. At the peak load ( $P_u$ ), the longitudinal strain ( $\epsilon_v$ ) of all circular aluminum alloy tubes was less than  $2400 \mu\epsilon$ , and the transverse strain ( $\epsilon_h$ ) was less than  $1200 \mu\epsilon$ , both of which were lower than the yield strain ( $\epsilon_y = 5460 \mu\epsilon$ ) calculated from the aluminum alloy material properties test data. The results indicate that the aluminum alloy tube was in the elastic deformation stage during the test. When the applied load reaches its peak, owing to the elastic characteristics of the material, the aluminum alloy tube begins to revert to its original shape, thereby exhibiting elastic recovery. This phenomenon results in a reduction in strain. Except for specimen  $\text{CCS120} \times 2.5\text{T}$ , the other circular tubes exhibited the pattern of  $S3 > S2 > S1$  for both  $\epsilon_v$  and  $\epsilon_h$  before reaching the peak load.

Figure 7 shows the load-strain ( $P$ - $\epsilon$ ) relationship curve for square specimens. Unlike circular sections, the strain at the corners of the square aluminum alloy tube was measured to compare the difference between the strain at the middle and the corners. The  $\epsilon_v$  and  $\epsilon_h$  of all square aluminum alloy tubes were lower than the measured strains of the circular tubes, and also lower than the compressive yield strain of the square tubes ( $\epsilon_y = 4890 \mu\epsilon$ ), indicating that the aluminum alloy tube remained in the elastic stage throughout the entire test. Before reaching the peak load, the strain change at the middle of the square aluminum alloy tube was consistent with that of the circular aluminum alloy tube, but there was no obvious pattern for the measurement points at the corners, indicating that the interface relationship between the corner of the square aluminum alloy tube and the concrete was more complex<sup>50,51</sup>.

### Strain distribution at different stages

To further analyze the strains discussed in section “Load-strain relationship curves”, Figs. 8 and 9 illustrate the strain distribution of the aluminum alloy tube at different loading stages. The specimen height  $H$  on the vertical axis is based on the orientation of the specimen during the test, where  $H = 0$  mm represents the free end and the other side represents the loading end. The specimen height ( $H$ ) was based on the orientation of the specimen during the test, where  $H = 0$  mm represents the free end and the other side represents the loading end. Figure 8 reveals that from the initial loading stage to the peak load, except for the  $\text{CCS120} \times 2.5\text{T}$  specimen (Fig. 8a), the transverse and longitudinal strains of the other specimens (Fig. 8b–c) show an increasing trend from the loading end to the free end. This could be due to the concrete not being vibrated densely during the pouring

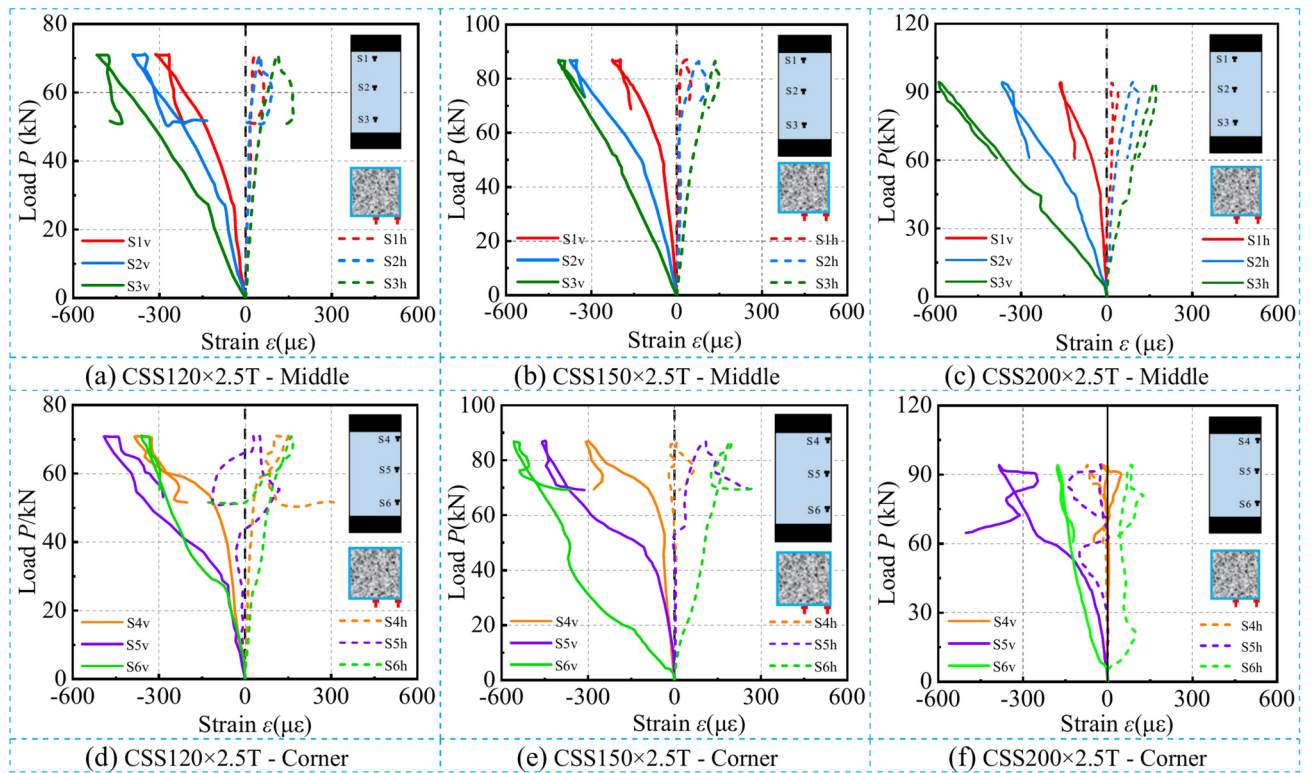


Fig. 7. Load-strain relationship curves of the square specimens.

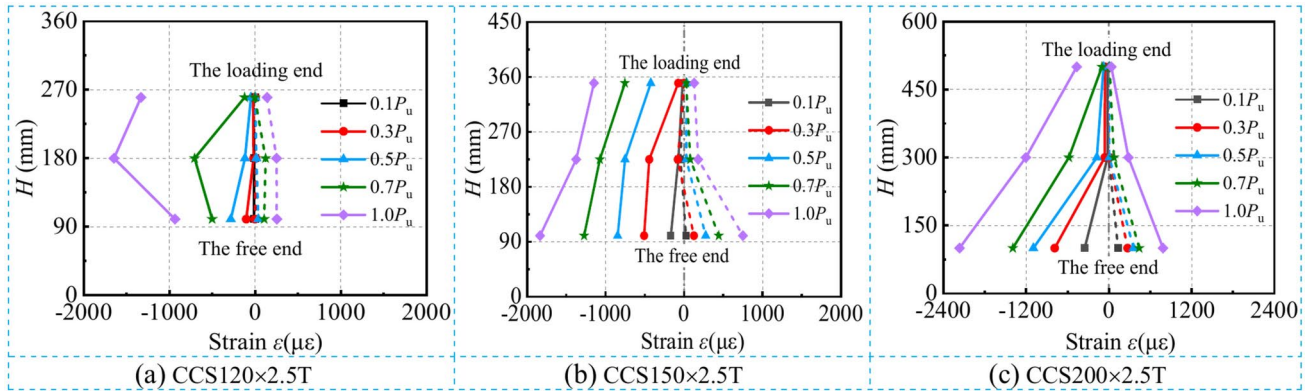


Fig. 8. Strain distribution at different loading stages of circular specimens.

process, resulting in voids in the middle of the concrete, which easily become areas of stress concentration when subjected to force. At the same time, the trend also satisfies the distribution law of exponential function.

As shown in Fig. 9, the longitudinal strain distribution at different stages in the middle of the square section is basically consistent with that of the circular section, also following the exponential function development pattern. However, at the corners of square sections, due to the corner effect, there are residual stresses after cold bending processing, so the change of corner strain is more complicated. Therefore, it is temporarily not possible to describe their strain distribution relationship through function fitting. This paper only studies the strain in the middle part of the square-section specimen.

### Interface bonding mechanism Longitudinal strain fitting

Based on the changes in the longitudinal strain ( $\epsilon_v$ ) of the aluminum alloy tube observed in Figs. 8 and 9 under different load levels, it is found that  $\epsilon_v$  follows an exponential function distribution. Therefore, an exponential function is used to fit the  $\epsilon_v$  distribution of the aluminum alloy tube as described in Eq. (2)

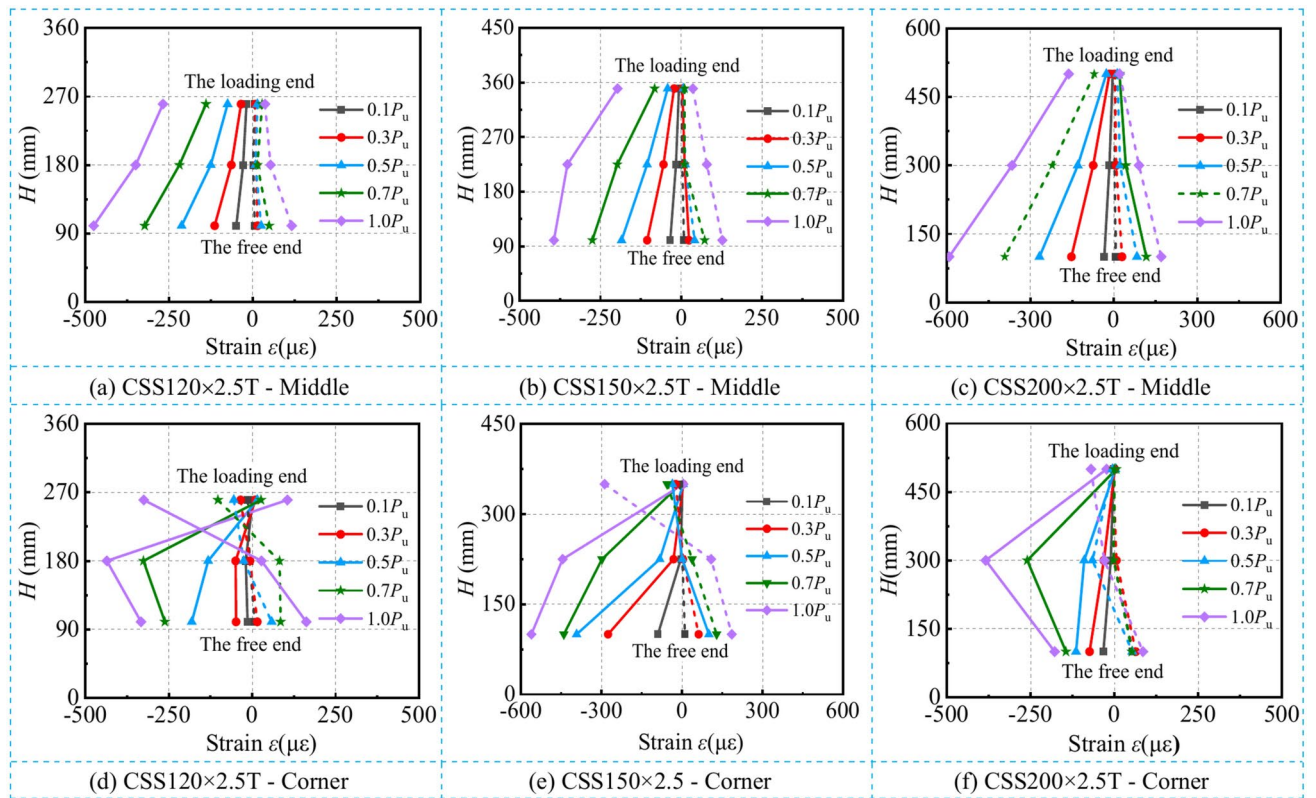


**Fig. 9.** Strain distribution at different loading stages of square specimens.

$$\varepsilon(x) = Ae^{Bx} \tag{2}$$

where the values of A and B are related to the load level, and their specific numerical values as shown in Fig. 10. From Fig. 10, it is observed that the fitting curves were essentially a negative exponential function, exhibiting the characteristic that the  $\varepsilon_v$  was maximum at the free end and gradually decreases towards the loading end. Apart from the fitting curve of specimen CCS120 × 2.5 T (Fig. 10a), the goodness of fit (R2) for other specimens (Fig. 10b–f) of the fitting curves is greater than 0.9. The results indicate that the fitting curves are close to the tested results, and the derived fitting formulas can accurately describe the variation of  $\varepsilon_v$  in the aluminum alloy tube at different positions along the specimen under different load levels.

**Interfacial bonding stress distribution**

The bond stress value at the CFAT column interface increases with the increase of load in the push-out specimen, and its distribution on the interface is relatively complex. Therefore, a study was conducted on the distribution pattern of bond stress along the transfer length of the aluminum alloy tube generated by CFAT, Fig. 11 shows the mechanical simplification analysis of the interface bond stress of CFAT. Taking a micro-element of the aluminum alloy tube, during the push-out test, the push-out force acting on the concrete surface will generate an upward interfacial bond stress on the concrete, while the bond stress on the aluminum alloy tube interface is the reaction force of the concrete interfacial bond stress. At this moment, the aluminum alloy tube is in equilibrium under the action of the push-out force and the bond stress. The equilibrium equation is as follows:

$$A_a d\sigma_a(x) = \tau(x)l_a dx \tag{3}$$

where  $A_a$  is the cross-sectional area of the aluminum alloy tube,  $d\sigma_a(x)$  is the incremental longitudinal stress of the aluminum alloy tube per unit length,  $l_a$  is the inner circumference of the aluminum alloy tube,  $\tau(x)$  is the bond stress value at this position from the free end, and  $dx$  is the incremental longitudinal length of the aluminum tube.

Since the aluminum alloy tube remains in the elastic stage during the push-out test, according to Hooke’s Law ( $\sigma_a = E_a \varepsilon_a$ ), the following expression can be derived:

$$\tau(x) = \frac{A_a E_a}{l_a} \frac{d\varepsilon(x)}{dx} \tag{4}$$

where  $\varepsilon(x)$  and  $E_a$  are the longitudinal strain and the elastic modulus of the aluminum alloy tube.

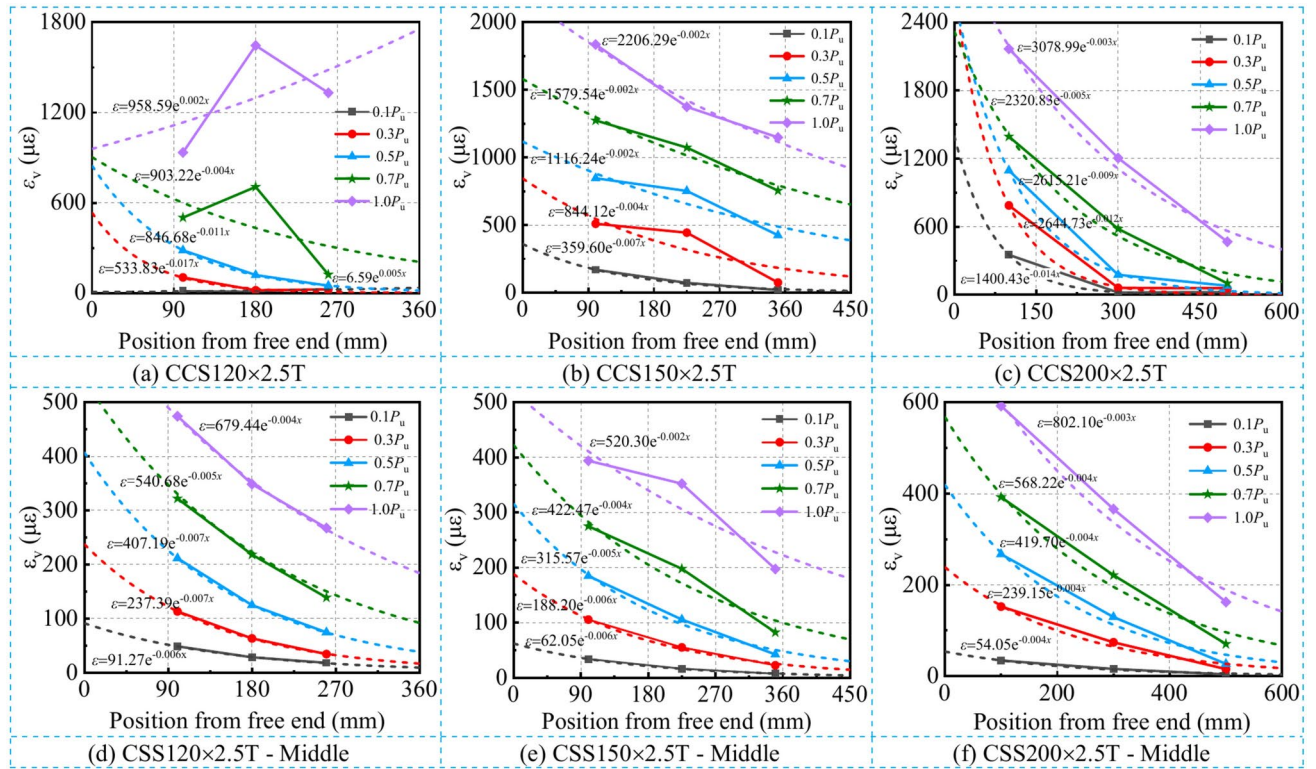


Fig. 10. The fitting curves of longitudinal strain.

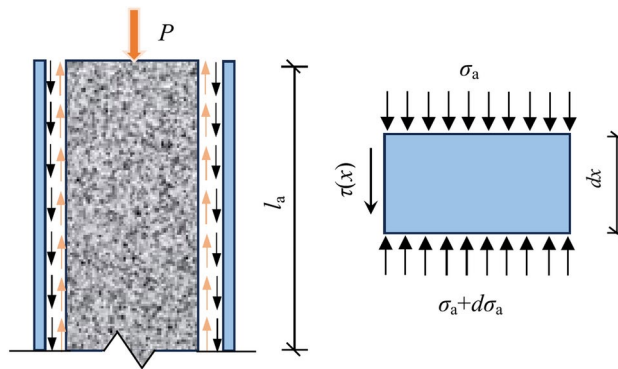


Fig. 11. Schematic diagram of the force on the push-out specimen and the aluminum alloy tube micro-element.

By substituting the longitudinal strain fitting equation from Fig. 10 and the relevant material parameters of the aluminum alloy tube into Eq. (4), the distribution of bond stress (Eq. 5) along the length of the aluminum alloy tube under different load levels before bond failure occurs is obtained, as shown in Fig. 12. The results indicate that the bond stress at the interface of the aluminum alloy tube follows the same pattern as the longitudinal strain.

$$\tau(x) = E_{at} \frac{d\varepsilon(x)}{dx} = E_{at} \frac{d(A\varepsilon^{Bx})}{dx} = AB E_{at} \varepsilon^{Bx} \tag{5}$$

### Bond slip constitutive relationship Existing model

At present, only the prediction formula for the bond strength of CFAT columns has been studied in Ref. 46, but it was only applicable to circular CFAT columns under high temperature. Therefore, in order to obtain the bond-slip constitutive relationship of CFAT columns, the bond performance of CFAT and CFST was compared, as shown in Fig. 13. Overall, the bond strength of CFST is higher than that of CFAT columns. This may be due

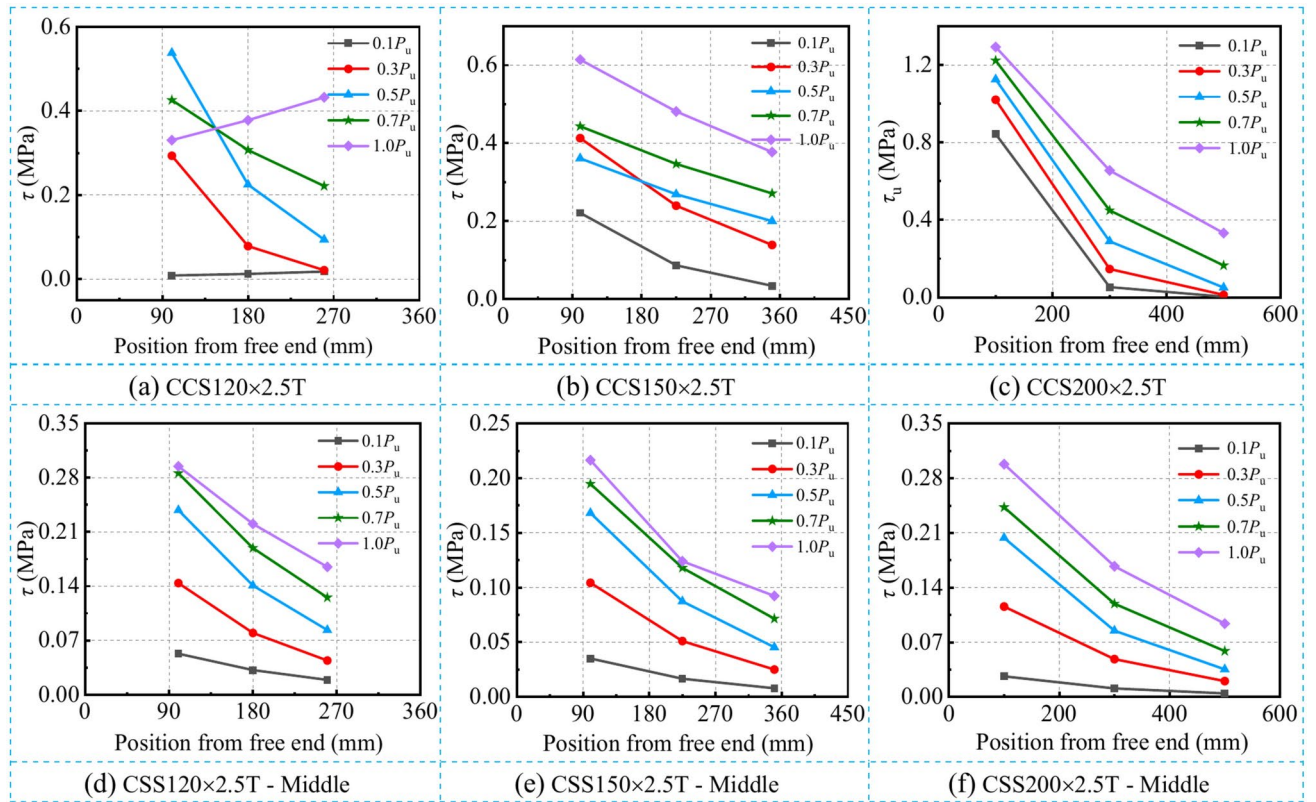


Fig. 12. Interfacial bonding stress distribution.

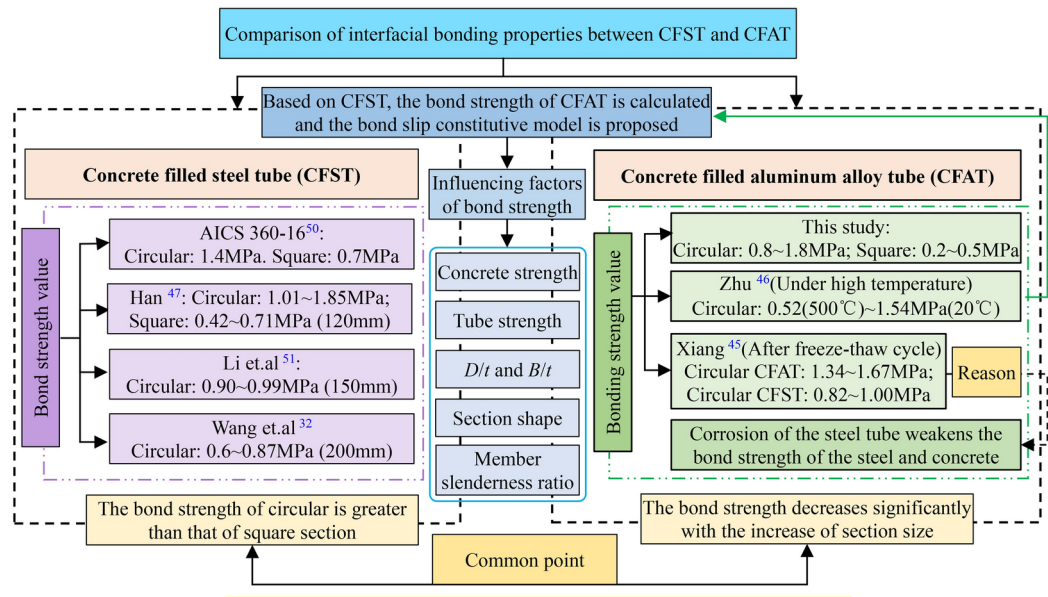


Fig. 13. Comparison of interfacial bonding properties between CFST and CFAT.

to the smooth surface of the aluminum alloy tube, which leads to a weaker mechanical bite force between the aluminum alloy tube and the concrete. Meanwhile, considering the similarity in the research on bond strength between CFST and CFAT columns, this paper summarizes three existing formulas for calculating the bond strength of CFST columns, providing a reference for future research on the bond-slip constitutive behavior of CFAT columns.

*Two-stage model*

Shakir-Khalil<sup>52</sup> proposed an ideal elastoplastic constitutive model (Fig. 14a) to describe the bond-slip behavior of CFST members. The model sets the ultimate bond strength  $\tau_u = 0.8$  MPa, corresponding to a slip value  $S_u = 0.5$  mm. The bond-slip model of CFST members is described using Eq. (6), and it's stipulated that the interfacial shear modulus ( $G_s = \tau_u/S_u$ ) has a uniform value of 0.165 MPa.

$$\tau = \begin{cases} G_s S & (0 < S \leq S_u) \\ \tau_u & (S > S_u) \end{cases} \quad (6)$$

*Three-stage model*

In the process of studying the  $\tau$ - $S$  curves of CFST members, it is commonly observed that the bond-slip relationship between the steel tube and core concrete exhibits a stress reduction phase after reaching peak stress. To more accurately characterize the unloading behavior of the members after peak stress, Liu<sup>53</sup> and Dong et al.<sup>54</sup> proposed a three-segment bond-slip model (Fig. 14b) to describe the bond-slip phenomenon in CFST. Liu<sup>53</sup> proposed Eq. (7) to describe the bond-slip behavior of CFST columns, based on an assumption that: after the peak point, the bond stress will linearly decrease by 35%, and when the  $\tau_r$  is reached, the slip  $S_u = 2.5\tau_u$ , while the residual bond strength corresponds to the slip  $S_r = 3S_u$ .

$$\tau = \begin{cases} 0.4S & (0 < S \leq S_u) \\ 1.2\tau_u - 0.2\frac{\tau_u}{S_u}S & (S_u < S \leq S_r) \\ 0.6\tau_u & (S > S_r) \end{cases} \quad (7)$$

*Four-stage model*

In order to describe the bond slip characteristics of CFST columns at the elastoplastic stage, Guan et al.<sup>55</sup> proposed a four-stage bond slip constitutive model (Fig. 14c). Parameters a, b, c and d in the figure were determined by the control points (A, B, C and coordinates at  $\tau_{0.5}$ ) of the test curve at different stages, and the model expression is shown in (8).

$$\begin{cases} S = 0 & (0 \leq \tau \leq \tau_s) \\ \tau = \tau_s + \frac{S}{aS+b} & (0 < S \leq S_u) \\ \tau = \frac{S}{cS+d} & (S_u < S \leq S_r) \\ \tau = \tau_r & (S > S_r) \end{cases} \quad (8)$$

Compared with three slip constitutive models, based on the  $\tau$ - $S$  curve in this study and accuracy, a three-stage model was adopted to describe the bond slip of CFAT columns. To obtain the two key control points ( $\tau_u, S_u$ ) and ( $\tau_r, S_r$ ), it's necessary to derive the characteristic bond strength values  $\tau_u$  and  $\tau_r$ , as well as the characteristic bond slip values  $S_u$  and  $S_r$  by design formulas. It is worth noting that a corresponding three-stage constitutive model for the bond stress-slip behavior of the interface between aluminum alloy tube and concrete after high temperature exposure was also proposed in Ref.<sup>46</sup>, which coincides with the approach adopted in this paper.

**Numerical calculation of key point**

*Ultimate bond strength and slip*

Figure 15a and b shows the effects of  $D(B)/t$  on the ultimate bond strength ( $\tau_u$ ) and bond slip ( $S_u$ ), respectively. For the circular specimens, when  $D/t$  increased from 48.0 to 60.0,  $\tau_u$  and  $S_u$  decreased by 14.2% and 19.3%, respectively. When  $D/t$  increased from 60.0 to 80.0,  $\tau_u$  and  $S_u$  decreased by 26.0% and 13.5%, respectively. For the specimens, when  $B/t$  increased from 48.0 to 60.0,  $\tau_u$  and  $S_u$  decreased by 25.5% and 15.7%, respectively. When  $B/t$  increased from 60.0 to 80.0,  $\tau_u$  and  $S_u$  decreased by 42.1% and 8.6%, respectively. It shows that the bond strength of CFAT is sensitive to the cross-sectional size. This is because in large-size specimens, the larger

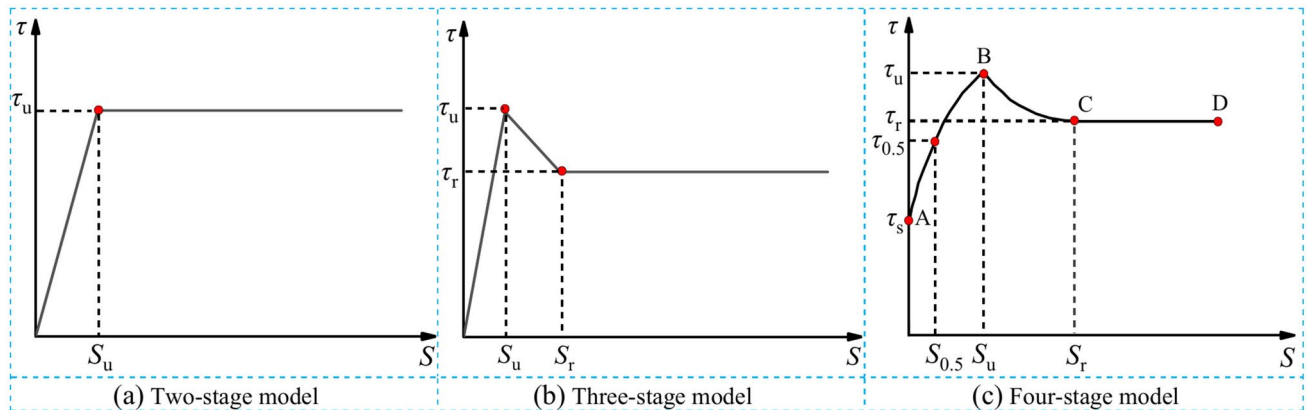


**Fig. 14.** Constitutive model of bond slip.

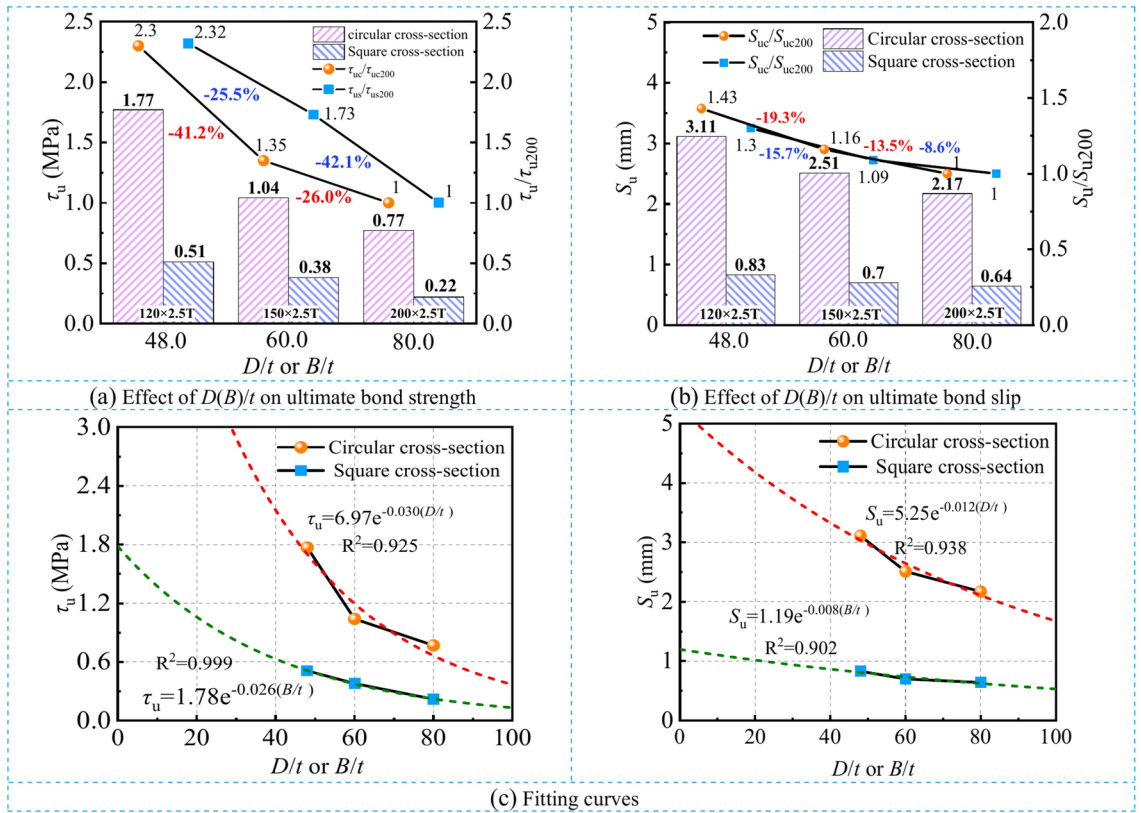


Fig. 15. Effect of  $D(B)/t$  on ultimate bond strength and slip.

volume of concrete leads to greater shrinkage, which increases the gap between the aluminum alloy tube and the concrete, thereby reducing the bond strength of the member. Secondly, when the thickness of the aluminum alloy tube is the same, in a small size tube, the aluminum alloy tube provides better confinement to the concrete, resulting in stronger interfacial bond strength. As the cross-sectional size increases, the confining effect of the aluminum alloy tube on the concrete weakens, leading to a reduction in interfacial bond strength.

Upon further observation, it was found that there is an exponential relationship between  $D(B)/t$  and  $\tau_u$ . By fitting them with exponential functions, the fitting formulas are shown in Eqs. (9) and (10). It was found that the goodness of fit ( $R^2$ ) of the fitting curves was greater than 0.9, as shown in Fig. 15c, indicating that the fitting formulas can accurately represent the relationship between  $D(B)/t$  and  $\tau_u$ .

$$\text{Circular cross-section : } \begin{cases} \tau_u = 6.97e^{-0.030(D/t)} \\ S_u = 5.25e^{-0.012(D/t)} \end{cases} \quad 48 < D/t < 60 \quad (9)$$

$$\text{Square cross-section : } \begin{cases} \tau_u = 1.78e^{-0.026(B/t)} \\ S_u = 1.19e^{-0.008(B/t)} \end{cases} \quad 48 < B/t < 60 \quad (10)$$

*Residual bond strength and slip*

The formulas (9) and (10) for calculating the ultimate bond strength of CFAT specimens have been provided, and the accuracy of these formulas has been further verified. However, the calculation of another characteristic bond strength value, still needs to be defined. In this study, refer to Liu<sup>53</sup> definition of the residual bond strength ( $\tau_r$ ). For circular specimens,  $\tau_r$  is defined as the value when the ultimate bond strength  $\tau_u$  decreased by 35%; for square specimens,  $\tau_r$  is defined as the values when the ultimate bond strength  $\tau_u$  decreased by 30%. Simultaneously, by fitting the relationship between the residual bond slip ( $S_r$ ) and  $D(B)/t$ , it was found that the circular specimens exhibited a linear relationship while the square ones exhibited a positive exponential relationship (Fig. 16). The calculation formulas are as follows:

$$\text{Circular cross-section : } \begin{cases} \tau_r = 0.65\tau_u = 4.53e^{-0.030(D/t)} \\ S_r = 4.39 + 0.26(D/t) \end{cases} \quad (11)$$

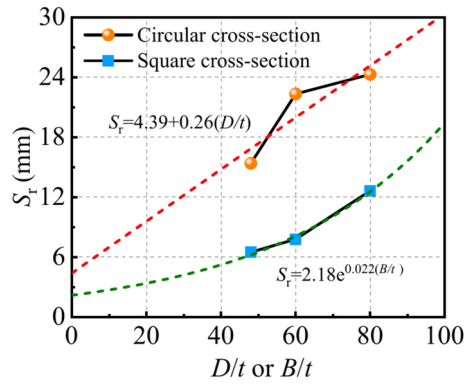


Fig. 16. Fitting of the functional relationship between  $D(B)/t$  and  $S_r$ .

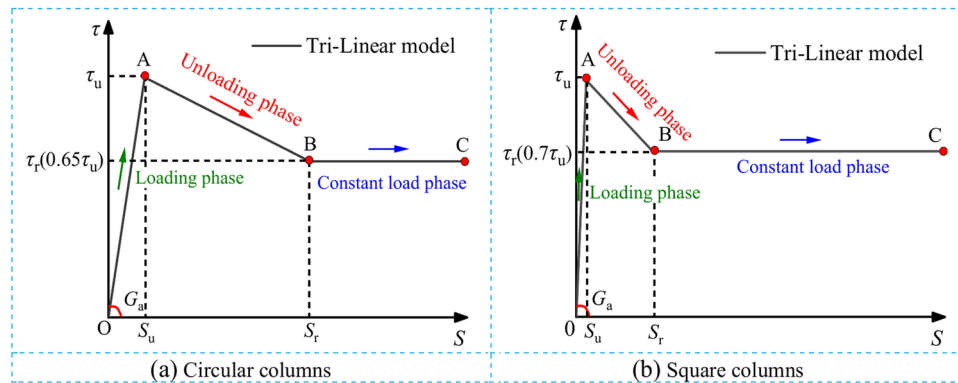


Fig. 17. Bond-slip ( $\tau$ - $S$ ) constitutive model.

$$\text{Square cross-section : } \begin{cases} \tau_r = 0.7\tau_u = 1.25e^{-0.026(B/t)} \\ S_r = 2.18e^{0.022(B/t)} \end{cases} \quad (12)$$

**Bond-slip constitutive model**

In order to understand the change rule of bonding force, it is assumed the bonding force is uniformly distributed at any time. The bond strength and bond slip eigenvalues were calculated by the formula, and a model of the bond slip constitutive relationship of CFAT column is proposed. The models and formulas can serve as reliable bases for subsequent finite element (FE) simulation validations, as shown in Fig. 17. In the OA stage, when the bond strength is less than the ultimate bond strength  $\tau_u$ , the slip value increases approximately linearly with the bond strength, but the rate of increase is higher for square sections than for circular sections. After point A, the stiffness of the curve changes from positive to negative. During the process of resisting slip, static friction disappears and turns into kinetic friction to provide resistance. The sliding friction plays an important role in the AB stage. The interfacial bonding force disappears and the surface has only kinetic friction force after point B, and the slope of the curve tends to 0. The expression is as follows:

$$\begin{cases} \tau = G_a S & (0 < S < S_u) \\ \tau = m(S - S_u) + \tau_u & (S_u < S < S_r) \\ \tau = n\tau_u & (S > S_r) \end{cases} \quad (13)$$

where  $G_a$  is the bond-slip stiffness,  $G_a = \tau_u/S_u$ .  $\tau_u$  and  $S_u$  are the ultimate bond strength and bond slip value. Circular section:  $m = 0.35\tau_u/(S_u - S_r)$  and  $n = 0.65$ ; the square section:  $m = 0.3\tau_u/(S_u - S_r)$  and  $n = 0.7$ .

From Fig. 18 can be observed that the calculated curves showed good agreement with test curves. Therefore, the proposed bond-slip constitutive model can accurately reflect the main trends of CFAT columns at different stages.

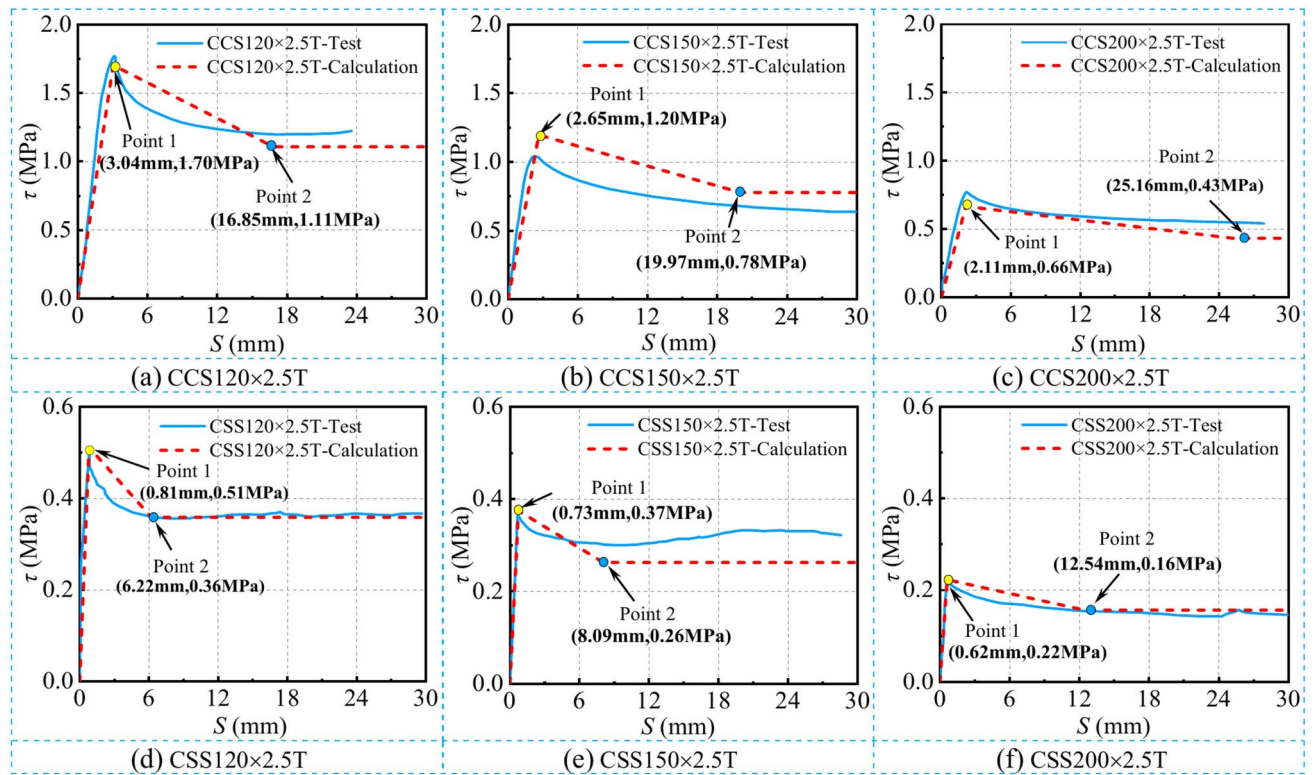


**Fig. 18.** Comparison of calculated and test results.

## Finite element analysis

### Finite element model

#### Element type and mesh size

A numerical model of the CFAT specimen was established using ABAQUS software, where both the aluminum alloy tube and the core concrete were modeled using solid elements (C3D8R), and the CFRP was modeled using shell elements (S4R). Due to the requirement that the spring setup necessitates a consistent mesh size for both the concrete and the aluminum alloy tube, structured mesh was used for partitioning. Specifically, to enhance the accuracy of the simulation results, the wall of the aluminum alloy tube was divided into two layers for mesh generation.

#### Interaction and boundary conditions

##### (1) Spring element model

Since the core concrete inside the aluminum alloy tube only slips along the axial direction of the specimen, the bond-slip behavior between the aluminum alloy tube and the core concrete can be simulated by arranging two-node spring elements (Spring 2) on their contact surface, and the free end 50 mm without spring. The arrangement of the springs and the boundary conditions are shown in Fig. 19.

##### (2) Cohesion model

For circular columns, surface to surface contact was used between the aluminum alloy tube and the core concrete, and the square columns, node to surface contact was used between the two. The concrete side surface with high stiffness is the main surface, and the aluminum alloy inner surface is the secondary surface. Since this simulation involves interface bonding slip, small sliding is set for both circular and square interfaces. In the coulomb friction model, hard contact is used to define normal behavior, penalty function is used to define tangential behavior, and the friction coefficient is 0.25.

## Material constitutive

### Aluminum alloy

The constitutive relationship of the aluminum alloy may be explained using the Ramberg–Osgood (R–O) model<sup>56</sup>. Gardner and Ashraf<sup>57</sup> discovered that when the strain is more than 0.5%, the R–O model predicts the stress of aluminum alloy to be higher than the actual stress, and then the model is improved. The expression is as follows:

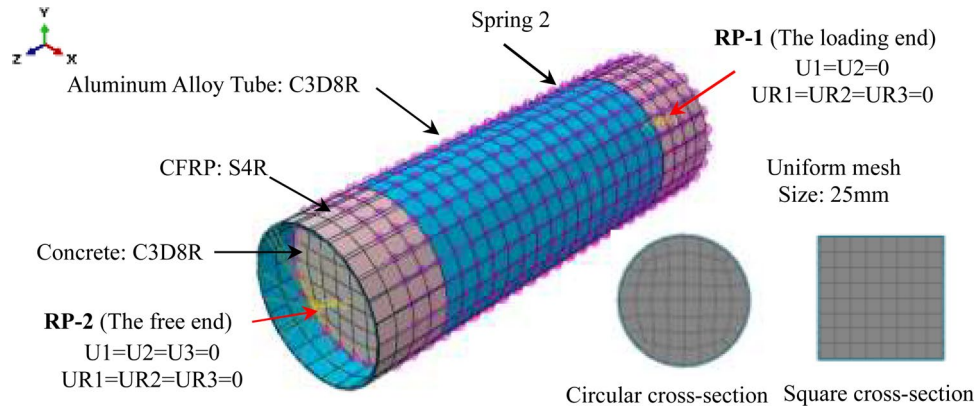


**Fig. 19.** Finite element (FE) model of CFAT push-out specimen (Images source: ABAQUS 2021. <https://www.3ds.com/products-services/simulia/products/abaqus/>).

$$\varepsilon = \begin{cases} \frac{f}{E_a} + 0.002 \left(\frac{f}{f_{0.2}}\right)^n & f \leq f_{0.2} \\ \frac{f-f_{0.2}}{E_{0.2}} + \left(\varepsilon_{0.1} - \varepsilon_{0.2} - \frac{f_{0.1}-f_{0.2}}{E_{0.2}}\right) \left(\frac{f-f_{0.2}}{f_{0.1}-f_{0.2}}\right)^{n'0.2,1.0} + \varepsilon_{0.2} & f > f_{0.2} \end{cases} \quad (14)$$

where  $\varepsilon$  and  $f$  are the strain and stress of aluminum alloy respectively,  $E_a$  and  $f_{0.2}$  are the initial elastic modulus and nominal yield strength corresponding to 0.2% residual strain of aluminum alloy respectively,  $n=f_{0.2}/10$  is the strain hardening index,  $E_{0.2}=E_a/(1+0.002nE_a/f_{0.2})$  is the tangent stiffness under  $f_{0.2}$ ,  $f_{0.2}$  and  $f_{1.0}$  are the nominal strengths corresponding to 0.2% and 1% strain, respectively,  $\varepsilon_{0.2}$  and  $\varepsilon_{1.0}$  are the strain values corresponding to  $f_{0.2}$  and  $f_{1.0}$ , respectively,  $n=20$ ,  $n'0.2, 1.0=4.5$  is the strain hardening coefficient<sup>57</sup>, which means nonlinearity of the stress–strain response between  $f_{0.2}$  and  $f_{1.0}$  is characterized.

**Concrete**

The stress–strain relationship for concrete in CFAT columns proposed by Han<sup>47</sup> was used, which takes into account the confinement effect, as described in Eq. (15). Moreover, the research by Wang et al.<sup>7</sup> has demonstrated that this model is suitable for simulating CFAT short columns.

$$y = \begin{cases} 2x - x^2 & x \leq 1 \\ \frac{x}{\beta_0(x-1)^{\eta} + x} & x > 1 \end{cases} \quad (15)$$

where  $x=\varepsilon/\varepsilon_0$ ,  $y=\sigma/\sigma_0$ ,  $\sigma_0=f_c$ .  $\sigma$  and  $\varepsilon$  are the stress and the strain of concrete, respectively.  $\sigma_0$  and  $\varepsilon_0$  are the peak stress and the peak strain of concrete, respectively.

**CFRP**

CFRP is an anisotropic composite material with high tensile strength along the fiber direction and negligible compressive strength perpendicular to the fiber direction. Therefore, the performance of CFRP is designated as the “LAMINA” material type, and its constitutive relation can be expressed as Eq. (16).

$$\sigma_f = \begin{cases} E_f \varepsilon, & 0 < \varepsilon \leq \varepsilon_f \\ 0, & \varepsilon > \varepsilon_f \end{cases} \quad (16)$$

where  $E_f$  and  $\sigma_f$  are the elastic modulus and ultimate tensile stress of CFRP, respectively.

**Model validation**

Figure 20 shows a comparison between the test and the simulated curves of the push-out specimens. For the circular columns, the simulated curves of the spring element are basically consistent with the tested curves during the loading and constant load phases. However, during the unloading phase, the simulated curves are higher than the tested curves. The cohesive model exhibits higher stiffness during the loading phase, but it matches well with the tested curves during the unloading and constant load phases. For the square columns, the curves of both the spring element and the cohesive model are basically consistent with the tested curves during the loading phase. However, during the unloading and constant load phases, the curves of the two models are lower than the tested curves, indicating that both models can well simulate the initial deformation of the square section specimens.

In summary, compared to the cohesive zone model, the spring element model can more accurately simulate the curve before the peak load, but it poorly fits the nonlinearity of the descending stage. This is because a uniformity assumption was made for the bond-slip constitutive behavior of CFAT in Eq. 13. Moreover, the bond-slip constitutive model was converted into a load-slip constitutive model during the modeling process.

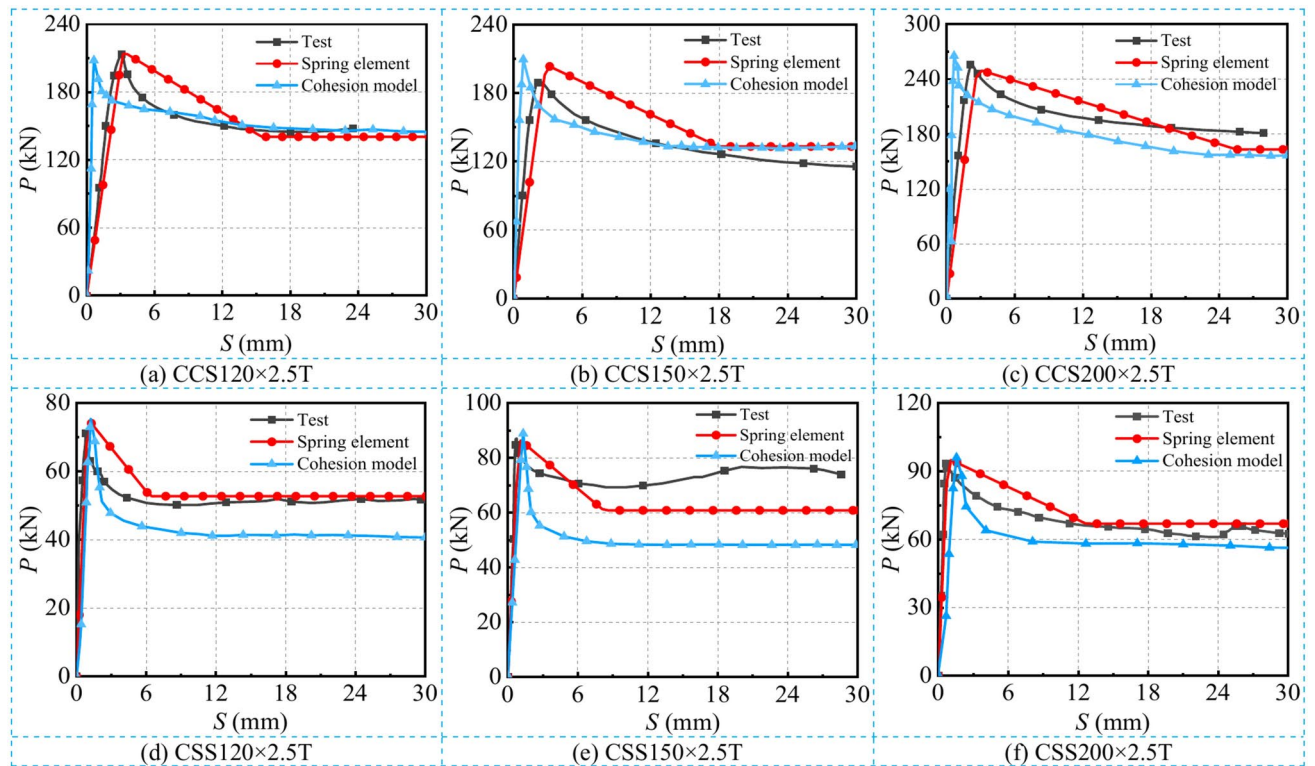


**Fig. 20.** Comparison of  $P$ - $S$  curves obtained by test and simulated.

### Stress distribution

The specimens obtained by the two different modeling methods showed no buckling phenomenon, and the stress cloud maps of the two methods were only slightly different in numerical values, so only the stress cloud maps obtained by the spring element modeling were shown.

#### Aluminum alloy

Figure 21 reveals that in the height direction of the aluminum alloy tube, the longitudinal compressive stress decreases from the free end towards the loading end. This is because during the loading process, the aluminum alloy tube is directly stressed at the free end first. Here, the compressive stress is the highest and decreases from bottom to top. According to the measured strain in the test and combined with the simulation results, it was found that the aluminum alloy tube remained in the elastic stage throughout the entire loading process. Based on the elastic assumption, the longitudinal strain of the aluminum alloy tube increases from the loading end towards the free end, which is consistent with the pattern observed in the experimental results.

The longitudinal stress of the circular aluminum alloy tube decreases from 233.81 MPa at the smallest section to 101.21 MPa at the largest section, and the square aluminum alloy tube decreases from 54.84 MPa at the smallest section to 45.80 MPa at the largest section. This is because as the section size increases, the bond strength between the aluminum alloy tube and the core concrete decreases, making it easier for the core concrete to be pushed. Meanwhile, the maximum longitudinal compressive stress of the square aluminum alloy tube is much smaller than that of the circular tube. This corresponds to the fact that the bond stress between the square aluminum alloy tube and the concrete is much lower than that of the circular tube, indicating the correctness of the simulation results.

#### Concrete

Figure 22 shows a comparison between the stress contour plot of the concrete at the loaded end section of a typical specimen and the experimental failure pattern. For the circular section, the maximum longitudinal stress is distributed in a symmetrically circular band around the outermost edge, corresponding to the crescent-shaped damage observed in the tested phenomena. However, since the FE model is an ideal model, it exhibits a symmetrically circular band. For the square section, the maximum longitudinal stress is distributed at the four corners, and the stress value in the middle of the section is also slightly greater than that at the core, corresponding to the experimental phenomenon where the concrete is severely damaged at the four corners and slightly damaged in the middle.

### Conclusion

In this study, the interfacial bond behavior of concrete-filled aluminum alloy tubes (CFAT) with square and circular specimens is analyzed by test and numerical simulation. The strain distribution of CFAT is analyzed.

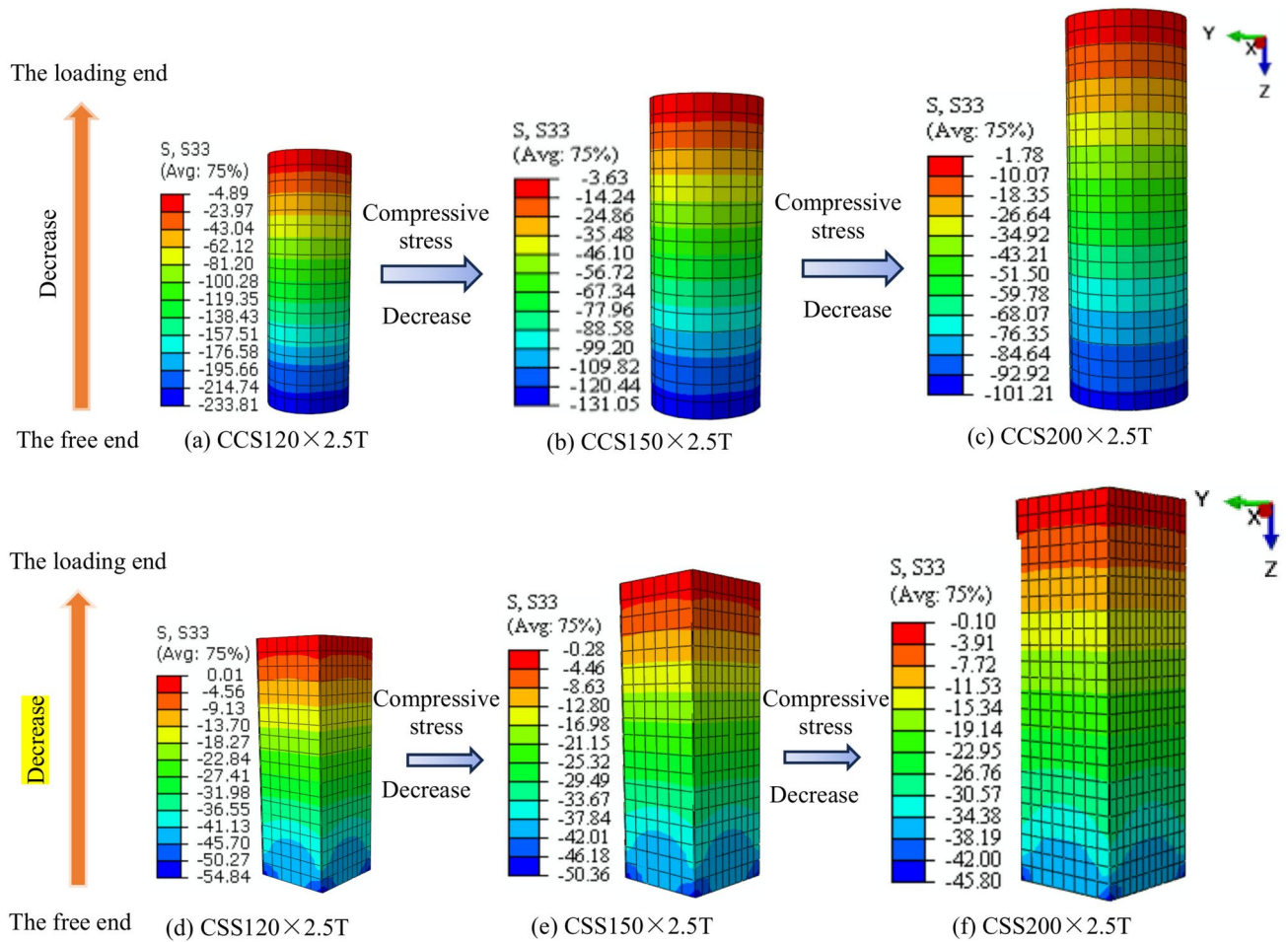


**Fig. 21.** Longitudinal stress distribution of aluminum alloy tube (Images source: ABAQUS 2021. <https://www.3ds.com/products-services/simulia/products/abaqus/>).

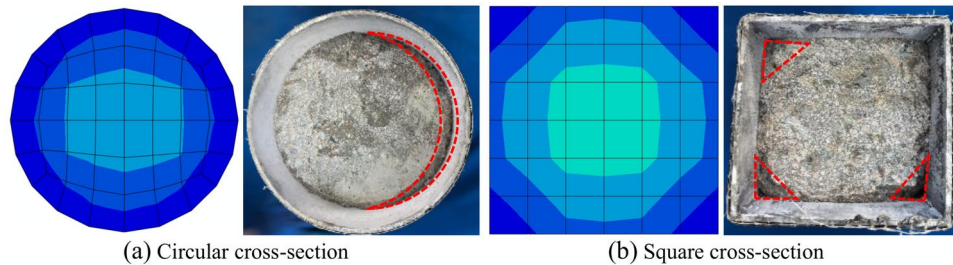


**Fig. 22.** Comparison of the loading end concrete (Images source: ABAQUS 2021. <https://www.3ds.com/products-services/simulia/products/abaqus/>).

A calculation formula for the ultimate bond strength of CFAT is proposed. Based on the proposed formula for characteristic points, a bond-slip constitutive model for CFAT columns is proposed and validated. The following conclusions are obtained:

- (1) The ultimate bond strength of circular CFAT ranged from 0.77 to 1.77 MPa, whilst square ones ranged from 0.22 to 0.51 MPa. In the loading process, the transverse and longitudinal strains of CFAT were lower than the yield strains. This indicates that the CFAT remains in the elastic stage throughout the entire loading process, and the longitudinal strain of the CFAT increased from the loading end towards the free end.
- (2) By fitting the longitudinal strain distribution of CFAT, the longitudinal strain presented a negative exponential function distribution rule. Based on the elastic assumption, the interfacial bond stress of CFAT was calculated.

- (3) As the diameter-to-thickness ratio ( $D/t$ ) or width-to-thickness ratio ( $B/t$ ) increased from 48.0 to 60.0, the ultimate bond strengths of square and circular CFAT decreased by 25.5% and 41.2%, respectively. As  $D/t$  or  $B/t$  increased from 60.0 to 80.0, the ultimate bond strengths of square and circular CFAT decreased by 42.1% and 26.0%, respectively. Meanwhile, a formula for calculating the bond strength of CFAT is proposed.
- (4) Based on the characteristic points of each stage and considering the differences in the characteristics of the bond-slip curves for square and circular columns, the bond-slip constitutive model for CFAT is proposed and validated. The calculation results are in good agreement with the tested results.
- (5) Based on the verified bond-slip constitutive model of CFAT, the finite element (FE) models of spring element and cohesive model are established, respectively. Using spring elements for simulation not only yields more accurate results but also has higher computational efficiency. However, the process of setting up the spring elements is relatively complex.

### Data availability

The data sets analysed during the current study are available from the corresponding author on reasonable request.

Received: 29 November 2024; Accepted: 24 February 2025

Published online: 10 March 2025

### References

1. He, K., Chen, Y., Tang, J. J. & Li, X. Post fire bond-slip performance of concrete-filled stainless steel tube columns. *Thin-Walled Struct.* **204**, 112275 (2024).
2. Chen, Y., Feng, R., Shao, Y. & Zhang, X. T. Bond-slip behaviour of concrete-filled stainless steel circular hollow section tubes. *J. Constr. Steel Res.* **130**, 248–263 (2017).
3. Zakaib, S. & Fam, A. Flexural performance and moment connection of concrete-filled GFRP tube-encased steel I-sections. *J. Compos. Constr.* **16**(5), 604–613 (2012).
4. Zhou, F. & Young, B. Concrete-filled aluminum circular hollow section column tests. *Thin-Walled Struct.* **47**(11), 1272–1280 (2009).
5. Zhou, F. & Young, B. Tests of concrete-filled aluminum stub columns. *Thin-Walled Struct.* **46**(6), 573–583 (2008).
6. Zhou, F. & Young, B. Numerical analysis and design of concrete-filled aluminum circular hollow section columns. *Thin-Walled Struct.* **50**(1), 45–55 (2012).
7. Wang, F. C., Zhao, H. Y. & Han, L. H. Analytical behavior of concrete-filled aluminum tubular stub columns under axial compression. *Thin-Walled Struct.* **140**, 21–30 (2019).
8. Patel, V. I., Liang, Q. Q. & Hadi, M. N. S. Numerical simulations of circular high strength concrete-filled aluminum tubular short columns incorporating new concrete confinement model. *Thin-Walled Struct.* **147**, 106492 (2020).
9. Zeng, X., Wu, W. B., Huo, J. S. & Hu, T. Study on axial compressive bearing capacity of short columns of circular aluminum alloy tube concrete. *Eng. Mech.* **38**(02), 52–60 (2021).
10. Jiang, M. Y. et al. Testing and numerical simulation of concrete-filled 6061-T6 aluminum tubular stub columns. *Structures*. **60**, 105855 (2024).
11. Wang, J. X., Liu, F. L. & Gao, S. Axial compressive behavior of aluminum alloy thin-walled tube confined concrete. *Constr. Build. Mater.* **467**, 140350 (2025).
12. Yan, X. F., He, M. N., Hao, J. P. & Lin, S. Q. Theoretical model of circular concrete-filled aluminum alloy tubular short columns under axial compression. *Eng. Struct.* **303**, 117549 (2024).
13. Yan, X. F., Ahmed, M. & He, M. N. Behavior and design of axially loaded high-strength concrete-filled circular aluminum tubular short columns. *Structures* **44**, 357–371 (2022).
14. He, Z. Y., Deng, Z. H., Hu, S. W. & Liu, B. Axial compression performance of coral concrete-filled aluminum alloy tube (CCFAT) circular short columns. *Eng. Struct.* **303**, 117552 (2024).
15. Deng, Z. H., Guo, J. H., Yu, J. J. & Liu, B. Axial compression performance of coral concrete-filled aluminium tube (CCFAT) square stub columns. *Case Stud. Constr. Mater.* **15**, e00697 (2021).
16. Guo, J. H., Wang, Y. M., Deng, Z. H. & Liu, B. Research on the axial compression performance of coral concrete-filled aluminum alloy tube columns. *Case Stud. Constr. Mater.* **20**, e02952 (2024).
17. Gkantou, M. et al. Geopolymer concrete-filled aluminium alloy tubular cross-sections. *Structures* **51**, 528–543 (2023).
18. Guler, S., Yavuz, D. & Aydin, M. Hybrid fiber reinforced concrete-filled square stub columns under axial compression. *Eng. Struct.* **198**, 109504 (2019).
19. Fayed, S. & Mansour, W. Structural performance of sea sand recycled aggregate concrete filled Solid/Hollow aluminum tubular Columns An experimental work. *Structures* **47**, 1323–1340 (2023).
20. Chen, Z. P., Xu, W. S. & Zhou, J. Mechanical performance of marine concrete filled CFRP-aluminum alloy tube columns under axial compression Experiment and finite element analysis. *Eng. Struct.* **272**, 114993 (2022).
21. Chen, Z. P. et al. Axial compressive performance and finite element analysis on spirally reinforced seawater sea-sand concrete-filled aluminum alloy tube columns. *Constr. Build. Mater.* **436**, 136927 (2024).
22. Zhou, F. & Young, B. Concrete-filled double-skin aluminum circular hollow section stub columns. *Thin-Walled Struct.* **133**, 141–152 (2018).
23. Zhou, F. & Young, B. Compressive strengths of concrete-filled double-skin (circular hollow section outer and square hollow section inner) aluminium tubular sections. *Adv. Struct. Eng.* **22**(11), 2418–2434 (2019).
24. Patel, V. I., Liang, Q. Q. & Hadi, M. N. S. Numerical study of circular double-skin concrete-filled aluminum tubular stub columns. *Eng. Struct.* **197**, 109418 (2019).
25. Ye, Y., Wang, L., Zhang, S. J. & Zhang, C. Y. Compressive behavior of concrete-filled aluminum alloy tube (CFAAT) stub column with inner carbon steel tube. *Structures* **32**, 701–712 (2021).
26. Zeng, X., Ning, C. Z., Zeng, W. Z. & Xu, B. Numerical and experimental studies on bending behavior of circular aluminium-concrete-steel double skin tubular cross-sections and bending capacity design approach. *J. Build. Eng.* **91**, 109524 (2024).
27. Gao, X. F., Zhang, Z. Y., Xu, J. & Su, S. Mechanical behavior of CFRP confined seawater sea-sand recycled concrete-filled circular aluminum-alloy tube columns under axial compression. *Constr. Build. Mater.* **397**, 132355 (2023).
28. Yang, H. Y. & Jiang, H. Experimental study on axial compressive performance of short concrete columns with CFRP-constrained aluminum alloy circular tubes. *Build. Struct.* **52**(S2), 1362–1368 (2022).
29. Chen, L. H. et al. Refining bond-slip constitutive relationship between checkered steel tube and concrete. *Constr. Build. Mater.* **79**, 153–164 (2015).

30. Gao, S. Life cycle sustainability assessment of concrete-filled steel tubular frames in earthquake regions. *Eng. Struct.* **328**, 119761 (2025).
31. Zhong, T., Song, T. Y., Uy, B. & Han, L. H. Bond behavior in concrete-filled steel tubes. *J. Constr. Steel Res.* **120**, 81–93 (2016).
32. Wang, F. C., Xie, W. Q., Li, B. & Han, L. H. Experimental study and design of bond behavior in concrete-filled steel tubes (CFST). *Eng. Struct.* **268**, 114750 (2022).
33. Yan, J. B., Xie, W. J., Zhang, L. X. & Lin, X. C. Bond behaviour of concrete-filled steel tubes at the arctic low temperatures. *Constr. Build. Mater.* **210**, 118–131 (2019).
34. Song, T. Y. et al. Bond behavior of concrete-filled steel tubes at elevated temperatures. *J. Struct. Eng.* **143**(11), 04017147 (2017).
35. Zhong, T., Han, L. H., Uy, B. & Chen, X. Post fire bond between the steel tube and concrete in concrete-filled steel tubular columns. *J. Constr. Steel Res.* **67**(3), 484–496 (2011).
36. Parsa-Sharif, M., Nematzadeh, M. & Bahrami, A. Post-fire load-reversed push-out performance of normal and lightweight concrete-filled steel tube columns Experiments and predictions. *Structures* **51**, 1414–1437 (2023).
37. Li, W., Chen, B. & Han, L. H. Pushout tests for concrete-filled double skin steel tubes after exposure to fire. *Thin-Walled Struct.* **176**, 109274 (2022).
38. Wang, W. D., Ma, W., Ji, S. H. & Shi, Y. L. Investigation on post-fire bond behavior between section steel and concrete in SRCFST columns[J]. *Structures* **69**, 107384 (2024).
39. Xu, K. C., Bi, L. P. & Chen, M. C. Experimental study of interfacial bonding stress-slip constitutive relationship of concrete-filled steel tube. *J. Build. Struct.* **36**(S1), 407–412 (2015).
40. Li, J. H., Wang, W. C., Zhou, C. H. & Chen, Z. H. study on the bond strength of concrete filled square steel tubes under freeze-thaw cycles environment. *Eng. Mech.* **41**(S1), 206–214 (2024).
41. Lu, Y. Y., Liu, Z. Z., Li, S. & Li, N. Bond behavior of steel fibers reinforced self-stressing and self-compacting concrete filled steel tube columns. *Constr. Build. Mater.* **158**, 894–909 (2018).
42. Cao, X., Xie, X. D., Zhang, T. Y. & Du, G. F. Bond-slip behavior between high-strength steel tube and ultra-high performance concrete. *Structures* **47**, 1498–1510 (2023).
43. Yang, Y. F., Zhang, L. & Dai, X. Performance of recycled aggregate concrete-filled square steel tubular columns exposed to fire. *Adv. Struct. Eng.* **20**(9), 1340–1356 (2017).
44. Liu, Z. Z., Lu, Y. Y., Li, S. & Xiao, L. Enhanced bond-slip behavior between recycled aggregate concrete and steel tubes under repeated loading. *Structures* **33**, 1263–1282 (2021).
45. Xiang, Q. Study on mechanical properties of concrete-filled metal tube beam-column joints after freeze-thaw cycle. Chongqing Jiaotong University (2019).
46. Zhu, M. Q. Study on mechanical properties of aluminum tube concrete medium long column under high temperature. China University of Mining and Technology (2023).
47. Han, L. H. *Concrete Filled Steel Tubular Structures-Theory and Practice* 4th edn. (Science Press, Beijing, 2022).
48. GB 50936-2014. Technical specification for concrete filled steel tube structure [S]. *Beijing: China Architecture and Construction Press*, (2014).
49. GB/T 228-2002, Room temperature tensile test method for metallic materials. Beijing China Standard Press (2002).
50. Gao, S., Yang, J., Kang, S.B., Li, F.Y. & Shi, X.N. Experimental and numerical studies on deformation performance of square concrete-filled steel tubular columns under repeated lateral impacts. *Eng. Struct.* **308**, 117909 (2024).
51. Gao, S., Peng, Z., Guo, L.H., Fu, F. & Wang, Y.G. Compressive behavior of circular concrete-filled steel tubular columns under freeze-thaw cycles. *J. Construct. Steel Res.* **166**, 105934 (2020).
52. Shakir-Khalil, H. Pushout strength of concrete-filled steel hollow sections. *J. Struct. Eng.* **71**(13), 234–241 (1993).
53. Liu, Y. Q. Theoretical analysis of the bond slip property of concrete-filled steel tube and verification by ANSYS program. Xi'an University of Architecture and Technology (2006).
54. Dong, H. Y., Chen, H. P., Cao, W. L. & Zhao, Y. Z. Bond-slip behavior of large high-strength concrete filled circular steel tubes with different constructions. *J. Constr. Steel Res.* **167**, 105951 (2020).
55. Guan, M. S., Lai, Z. C., Xiao, Q., Du, H. B. & Zhang, K. Bond behavior of concrete-filled steel tube columns using manufactured sand (MS-CFT). *Eng. Struct.* **187**, 199–208 (2019).
56. Ramberg, W. & Osgood, W.R. Description of stress-strain curves by three parameters. National Advisory Committee for Aeronautics (1943).
57. Gardner, L. & Ashraf, M. Structural design for non-linear metallic materials. *Eng. Struct.* **28**(6), 926–934 (2006).

## Acknowledgements

The authors would like to acknowledge the financially supported by the National Natural Science Foundation of China (No: 52368021, 52068047, 52278165), Lanzhou Youth Science and Technology Talent Innovation Project (No: 2023-QN-40), Hongliu Jieqing Talent Support Program Project of Lanzhou University of Technology, Industry Support Program Project of Gansu Provincial Department of Education (2024CYZC-16), Gansu Province Youth Talent Program Project, Outstanding Young Talents of Longyuan and Heilongjiang Science Fund for Excellent Young Scholars (YQ2023E023).

## Author contributions

Fangling Liu wrote the main manuscript text. Jingxuan Wang guided the conceptualization and writing of the original draft. Shan Gao provided the methodology and writing-view @ editing. All authors reviewed the manuscript.

## Declarations

## Competing interests

The authors declare no competing interests.

## Additional information

**Correspondence** and requests for materials should be addressed to J.-X.W. or S.G.

**Reprints and permissions information** is available at [www.nature.com/reprints](http://www.nature.com/reprints).

**Publisher's note** Springer Nature remains neutral with regard to jurisdictional claims in published maps and institutional affiliations.

**Open Access** This article is licensed under a Creative Commons Attribution-NonCommercial-NoDerivatives 4.0 International License, which permits any non-commercial use, sharing, distribution and reproduction in any medium or format, as long as you give appropriate credit to the original author(s) and the source, provide a link to the Creative Commons licence, and indicate if you modified the licensed material. You do not have permission under this licence to share adapted material derived from this article or parts of it. The images or other third party material in this article are included in the article's Creative Commons licence, unless indicated otherwise in a credit line to the material. If material is not included in the article's Creative Commons licence and your intended use is not permitted by statutory regulation or exceeds the permitted use, you will need to obtain permission directly from the copyright holder. To view a copy of this licence, visit <http://creativecommons.org/licenses/by-nc-nd/4.0/>.

© The Author(s) 2025